Aerospace Science and Technology 140 (2023) 108467

Contents lists available at ScienceDirect

Aerospace Science and Technology

journal homepage: www.elsevier.com/locate/aescte

Numerical and experimental analysis of fuel regression rate in a lab-scale hybrid rocket engine with swirl injection

Mario Tindaro Migliorino [a,*], Marco Fabiani [a], Christian Paravan [b], Daniele Bianchi [a], Francesco Nasuti [a], Luciano Galfetti [b], Rocco Carmine Pellegrini [c], Enrico Cavallini [c]

[a] Sapienza University of Rome, Via Eudossiana 18, 00184 Rome, Italy
[b] Politecnico di Milano, via La Masa 34, 20156 Milan, Italy
[c] Italian Space Agency, Via del Politecnico snc, 00133 Rome, Italy

ARTICLE INFO

Article history:
Received 31 March 2023
Received in revised form 31 May 2023
Accepted 16 June 2023
Available online 22 June 2023
Communicated by Damiano Casalino

Keywords:
Hybrid rockets
Swirl injection
Paraffin wax

ABSTRACT

In this work the regression rate performance and flow physics of a lab-scale hybrid rocket engine burning gaseous oxygen and paraffin-based fuels are experimentally and numerically investigated. Regression rates are obtained by thickness-over-time averaging procedures and through a non-intrusive optical method enabling fuel grain port diameter tracking. A numerical rebuilding of the experimental data is performed with axisymmetric Reynolds-averaged Navier-Stokes simulations, using sub-models accounting for the effects of turbulence, chemistry, radiation, and fluid-surface interaction. Simulations are performed with different computational setups, also considering the fuel grain shape variation over time, obtaining a fairly good agreement between the numerical and experimental data. A parametric analysis is also performed to assess the variation of the fuel regression rate with swirl intensity.

1. Introduction

Hybrid rocket engines (HREs) are propulsion devices burning a solid fuel and a liquid or gaseous oxidizer [1]. Despite being known since the 1930s [2], they have found limited applications in the past, mainly due to the low fuel regression rate [3], which limited the maximum thrust obtainable with an engine of given size. In the past years, however, significant improvements have been made in the field of hybrid propulsion, leading to a renovated interest of the industry, as testified by the flights of SpaceShipOne and Two [4] and by many European efforts, such as the SL1 launcher by Hympulse [5], and the EU 2020 HYPROGEO [6,7] and FLPP [8] programs of the European Space Agency.

One of the most important innovations was the introduction of liquefying fuels, namely fuels that form an unstable liquid layer on the burning surface, leading to droplet entrainment and to an increase in regression rate [9]. The most common liquefying fuel is paraffin wax, which allows to increase the regression rate up to 3-4 times with respect to conventional pyrolyzing fuels [4,10].

Pure paraffin wax has, however, low mechanical properties, requiring blending with reinforcing agents, such as thermoplastic and thermosetting polymers [11–15]. In this work, a thermoplastic polymer whose chain is composed by styrene, ethylene, styrene and butylene grafted with maleic anidride (SEBS-MA) is selected. A thorough rheological and ballistic characterization of the paraffin-SEBS blends has been performed.

To further increase both the fuel regression rate and the engine combustion efficiency, swirl injection may be used [16–26], injecting the oxidizer into the combustion chamber with a non-zero tangential component of velocity. It is in fact known that, in inert flows, swirl considerably increases the convective wall heat transfer [27] and it has been also proved to be one of the most effective means to improve flame stability and combustion efficiency in combustors and liquid rocket engines [28,29]. The effects of swirl motion depend on the rotational intensity of the flow, quantified by a dimensionless parameter, the *swirl number* [28], defined as

$$SN = \frac{\text{angular momentum flux}}{R_{\text{wall}} \times \text{axial momentum flux}} = \frac{\int_S (\rho u w r) dS}{R_{\text{wall}} \int_s (\rho u^2) dS} \tag{1}$$

where S is the cross section, r the distance from the axis, R_{wall} the wall radius, ρ the density, u the axial velocity and w the tangential velocity. This parameter is usually rewritten as a *geometric swirl number*, function of the sole geometry of the injector [30,31]

$$SN_g = \frac{\pi \left(R_{\text{wall}} - r_h\right) R_{\text{wall}}}{A_{\text{inj}}} \tag{2}$$

* Corresponding author.
E-mail address: mariotindaro.migliorino@uniroma1.it (M.T. Migliorino).

https://doi.org/10.1016/j.ast.2023.108467

Nomenclature

conv	convection	c	specific heat ..... J/(kg·K)
DD	diameter difference	D	diameter ..... m
end	final	G	mass flux ρu ..... kg/(m^{2}s)
grain	fuel grain	h	enthalpy per unit mass ..... J/kg
inj	injection	L	length ..... m
in	initial	p	pressure ..... Pa
MB	mass balance	q	heat flux ..... W/m^2
melt	melting	r	radius ..... m
ox	oxidizer	S	surface ..... m^2
poc	postchamber	SN	swirl number
pre	prechamber	SN_g	geometric swirl number
rad	radiation	T	temperature ..... K
TR	time resolved	t	time ..... s
$\dot{m}$	mass flow rate ..... kg/s	TMD	theoretical maximum density ..... kg/m^3
$\dot{r}$	fuel regression rate ..... mm/s	u	axial velocity ..... m/s
μ	dynamic viscosity ..... Pa·s	w	tangential velocity ..... m/s
ρ	density ..... kg/m^3	x	axial coordinate ..... m
A	area ..... m^2	y^+	dimensionless wall distance

where r_h is the radius of the injection channels and A_{inj} the injection area. This quantity allows to estimate the rotational intensity of the flow near the injector, before the effects of friction [32], mass adduction and energy release [33], and flow acceleration [28] lead to its decrease. It is known that SN_g is usually an overestimation of SN [34], due to the simplifying hypotheses [31] made in its definition.

Several firing tests [35,19,21–23,36] have shown that swirl injection leads to a considerable increase in regression rate, but there is still a relatively incomplete understanding of the relevant physical phenomena. Therefore, CFD simulations can be a useful tool in the analysis and design of swirl-injected HREs, providing insight on the internal flowfield and allowing to investigate different configurations without the need for complex and costly experiments.

In this paper, numerical efforts from Centro Ricerca Aerospaziale Sapienza (CRAS) of Sapienza University of Rome are joined with experimental investigations performed at the Space Propulsion Laboratory (SPLab) of Politecnico di Milano, in the framework of the PHAEDRA (Paraffinic Hybrid Advanced Engine Demonstrator for Rocket Application) project coordinated by the Italian Space Agency [37]. The work focuses on the analysis of the internal ballistics of a lab-scale hybrid rocket engine employing paraffin-based fuels.

The manuscript is organized as follows: the results of the experimental analysis are presented in Sec. 2; the computational model used for the simulations is summarized in Sec. 3; the employed computational setups are explained in Sec. 4 and the numerical results are presented in Sec. 5. In Sec. 6 the numerical model is extended to wax-SEBS fuel blends, on the basis of both experimental and numerical results.

2. Experimental setup and results

Burning tests are performed with a lab-scale hybrid rocket engine extensively described in Ref. [38]. Cylindrical grains with single central port perforation are tested. The experimental setup design enables sample head-end visualization during the burning. The main observable of interest is the solid fuel regression rate ($\dot{r}$). The latter is determined by thickness over time (TOT) method or by an optical time-resolved technique implemented at SPLab [39].

The oxidizer is injected by eight radial channels. The injector features SN_g = 3.3. Tested samples initial port diameter (D_0) is 5 mm, while the grain external diameter is 30 mm, thus, solid fuel web thickness is 12.5 mm. Fuel grain length is 50 mm. Combustion tests are performed with gaseous oxygen (GOX). Strand ignition is achieved by a solid propellant primer charge. Combustion chamber pressure is measured by a piezoresistive transducer placed in the engine pre-combustion chamber. The oxidizer mass flow rate $\dot{m}_{ox}$ is measured and controlled by a digital flowmeter. Tests are executed with oxidizer mass flow rate in the range 5 to 7.5 g/s.

2.1. Regression rate data reduction

Regression rate data reduction aims at the identification of a relationship between the regression rate and the oxidizer (or propellant) mass flux (G_{ox}, or G respectively). The $\dot{r}(G_{ox})$ is typically presented as a compact power law:

$$\dot{r}(G_{ox}) = a_r \cdot G_{ox}^{n_r} \tag{3}$$

Under given operating conditions, different data reduction methods may imply differences in the $\dot{r}$ values. In spite of this, the relative ballistic grading of the investigated fuel formulations is typically independent of the used data reduction technique.

2.1.1. Thickness over time method

Thickness over time provides time- and space-averaged regression rates. The method is applied on both diameter and mass changes in the burning time (Δt_b). The latter is defined based on combustion chamber pressure history [38]. Ignition is conventionally set at the time the combustion chamber pressure (p) increases due to the primer charge ignition. Burning test termination is achieved by a nitrogen purge commanded by electrovalves switching from oxidizer to inert gas flow. After ignition, Δt_b is in the range 3 to 5 s for all the performed tests. Given the different fuel regression rates, burning times are tailored to grant suitable average oxidizer mass fluxes for the relative grading of the formulations. Fig. 1a shows the pressure trace of a typical burning experiment, with the main test events highlighted and an indication of the Δt_b.

When based on port size change, the regression rate is expressed as the difference between the sample actual initial and final diameters [$D(t_{in})$ and $D(t_{end})$, respectively],

$$\dot{r}_{DD} = \frac{1}{\Delta t_b} \frac{D(t_{end}) - D(t_{in})}{2} \tag{4}$$

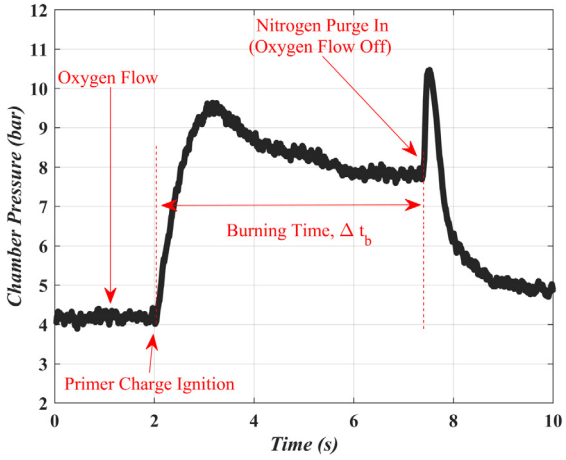

(a) Pressure history

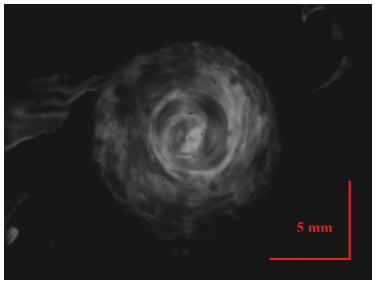

(b) Combustion run

Fig. 1. Burning test on the SPLab hybrid rocket engine: (a) typical pressure trace and test phases, (b) image captured from the combustion of paraffin in GOX. In (b), the vortex induced by the swirl radial injector is visible.

In the case of the mass balance, considering the theoretical maximum density (TMD), and the average fuel grain length (L_{grain}), the regression rate is given by

$$\dot{r}_{MB} = \frac{1}{\Delta t_b} \frac{2 \cdot [m(t_{in}) - m(t_{end})]}{TMD \cdot \pi \cdot [D(t_{in}) + D(t_{end})] \cdot L_{grain}} \tag{5}$$

where m is the measured fuel grain mass.

For both Eq. (4) and Eq. (5), the corresponding average oxidizer mass flux is defined as

$$\bar{G}_{ox,ave} = \frac{16 \cdot \dot{m}_{ox}}{\pi \cdot [D(t_{end}) + D(t_{in})]^2} \tag{6}$$

2.1.2. Time-resolved method

The SPLab time-resolved method for the regression rate (TR) is based on high-speed visualization of the combustion process (see Fig. 1b) [39]. The regression rate is determined based on the central port diameter sampling. Regression surface tracking starts from the frame at which the head-end central port diameter became visible (after primer charge ignition). Data sampling is extended until the end of the combustion (depending on visualization quality). Diameter sampling is performed with frequency in the range 2 to 10 Hz. Higher frequencies are used in the earlier phases of the burning process (faster regression rates), while slower samplings characterize the last part of the measurement (when surface regression is slowed down). During the combustion, the central port diameter is sampled along different radial directions (depending on combustion uniformity). The tracked diameter is the one identified from the head-end visualization of the specimen (see Fig. 1b). Effects such as the head-end consumption of the grain have no significant effects on the diameter sampling [39,40]. The local diameters were averaged to provide the instantaneous diameter at the given sampling time ($\bar{D}_i$). This diameter is considered uniform for the whole specimen length (given the relatively short grain longitudinal extension). The sequence of the $\bar{D}_i$ is a discrete information in time. This discrete sequence of sampled diameters and sampling times is made a continuous function by a power-law fitting

$$\bar{D}(t) = a_D \cdot (t - t_0)^{n_D} + D_0, \quad t \geq t_{ign} \tag{7}$$

The fitting of Eq. (7) is maximized by the use of the ad hoc defined ignition time (t_{ign}). The latter well suits the ignition conditions at small scale for the range of initial G_{ox} of interest [41]. The regression rate and oxidizer mass flux histories in time are evaluated starting from Eq. (7) as

$$\dot{r}(t) = \frac{1}{2} \cdot \frac{dD(t)}{dt} = \frac{1}{2} \cdot a_D \cdot n_D \cdot (t - t_0)^{n_D - 1} \tag{8}$$

$$G_{ox}(t) = \frac{4 \cdot \dot{m}_{ox}}{\pi \cdot [\bar{D}(t)]^2} \tag{9}$$

Consistency checks are applied for the evaluation of the time-resolved values, details are reported in Ref. [39]. The time-resolved method provides a regression rate characterization over a G_{ox} range with a single combustion run. Yet, different tests performed for the same fuel under fixed operating conditions can be collapsed in an ensemble average curve. For the latter, uncertainties are evaluated by considering confidence intervals with 95% accuracy. A minimum of three tests is considered for error bar definition in the ensemble average. In a dataset, it is possible that the TR method is applied to a reduced series of firings. This can be due to different reasons. First, the TR method requires that the operating conditions of the experimental runs are the same for the all the tests collapsed in an ensemble average (in particular, the initial G_{ox} and the strand geometry). In addition, in some cases the image quality is compromised by head-end burning/unclear recognition of the regressing surface and these factors limits the applicability of the method [39].

2.2. Tested fuels and pre-burning characterization

Tested fuel formulations are based on a commercial microcrystalline wax (SASOL 0907, TMD = 929 kg/m^3 here labeled as mWA). Paraffin is tested as it is, or blended with SEBS-MA (Sigma-Aldrich, TMD = 910 kg/m^3). Carbon powder (Sigma Aldrich, average particle size < 20 µm) is added to all the tested fuels (1 *wt%*) to prevent in-depth absorption of radiation heat transfer. The styrene copolymer is added to the compositions with mass fractions of 10 and 20 *wt%*. Details on the tested fuel formulations are given in Table 1. Other fuels have been considered (i.e. F3 and F4 formulations), but are not of interest in this work.

Preliminary thermal and mechanical characterizations of the tested fuels are reported elsewhere [42]. In this work, focus is on the melt fuel rheology due to its impact on the regression rate. Rheology tests are performed to determine the melt fuel viscosity under reference conditions (strain rate range 1-1000 s^{-1}, temperature 423 K).

Blending of mWA with SEBS-MA produces no significant effects on the TMD of the tested formulations. The same holds for the actual densities of the manufactured fuels, that are all within a ±3% of the theoretical value. On the other hand, the impact of the reinforcing polymer on the melt fuel viscosity is marked, as will be shown in Sec. 6. Cold flow visualizations at ambient pressure for melt layer temperature of 423 K are shown in [38]: viscosity

Table 1
Tested fuel formulations.

Fuel Id.	Composition	TMD, kg/m^3
F1	mWA (99 *wt%*) + C (1 *wt%*)	929
F2	mWA (89 *wt%*) + SEBS-MA (10 *wt%*) + C (1 *wt%*)	928
F5	mWA (79 *wt%*) + SEBS-MA (20 *wt%*) + C (1 *wt%*)	926

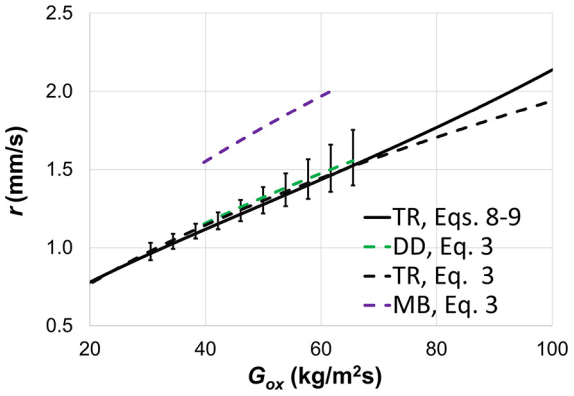

Fig. 2. F1 ballistic characterization: time-resolved and TOT data.

enhancement from F1 to F5 gradually suppresses the melt layer instability, with SEBS-MA addition at 20 *wt%* suppressing droplet detachment from the surface roll waves.

2.3. Ballistic characterization

Ballistic characterization is presented considering the TOT methods first, then time-resolved data are discussed.

Mass-based TOT shows faster regression rates than the DD counterpart. This is due to the head-end burning altering the grain length: the mass change accounts for this effect that is not captured by the simple diameter measurement. The increasing viscosity due to the SEBS-MA load implies a regression rate reduction of the blended fuel. Entrainment mass transfer suppression is the main cause for the slower recession of the surface. Focusing on F2, the percent regression rate difference (with respect to F1) is -43% when considering DD, and -47% for MB. For F5, the relative grading yields a -63% with DD, and -65% when using the MB method.

A deeper comparison of the ballistic responses of the fuels is possible by the power law fitting reported in the Table 2. Thickness over time data for F1 feature relatively low data fitting values due to the data scattering induced by the fuel mechanical properties. Independently of the reduction method (MB or DD), the n_r value of the power law fitting is close to the value of 0.6 typically found in the literature for the combustion of paraffin wax fuels [9]. The DD data feature a good agreement with the TR counterpart, as shown in Fig. 2. In the high G_{ox} region, Eq. (3) shows a relatively low fitting to the instantaneous data. This is an effect of the small port diameter of the samples inducing a relatively strong sensitivity to oxidizer mass flux in the earlier phases of the combustion process.

3. Computational model

The numerical simulations have been performed solving the Reynolds–averaged Navier–Stokes (RANS) equations [43], with submodels accounting for the effects of turbulence, chemistry, gas-surface interaction, and thermal radiation. In all simulations an axisymmetric approach has been used, with a periodic boundary condition on the lateral faces ensuring the symmetry of the flow. Such simulations can be used as a quick design tool, while, on the other hand, most of the work present in literature either employs 3D [44,45] or LES [46] simulations, which have high computational cost, or makes use of simplified injection approaches [18].

The numerical model is extensively described in [47,48] and the main details are reported below for the sake of completeness.

The simulations were performed with an in-house solver, validated in many different operating conditions [47–50]. The finite-volume computational tool is second-order accurate in time and employs a Roe Riemann solver [51], with the Strang operator-splitting technique used for time integration [52], through a second-order Runge-Kutta scheme for convective and diffusive terms and an implicit integrator for the chemical source terms. The specific isobaric heat, enthalpy and transport properties are expressed, as a function of temperature, using the polynomials taken from CEA database [53] for all species except paraffin, and the heats of formation as well. Wilke's rule [43] was used to obtain the mixture molecular transport properties, considering a constant Schmidt number $\mathrm{Sc} = 0.7$. The Prandtl number is computed from the mixture properties. The adopted turbulence model is the one of Spalart-Allmaras [54], with turbulent Prandtl and Schmidt numbers equal to 0.9 and 0.7.

A global reaction mechanism is employed to model the combustion of ethylene, which is the main product of paraffin cracking [55,56], adapting a model for the combustion of butadiene, due to the lack of literature data, consisting of seven reactions and ten species (Table 3). The forward reaction rates were computed through Arrhenius-type equations and the backward rates as the ratio between the forward ones and the equilibrium constant.

The paraffin taken into account in the present work is $C_{32}H_{66}$. Paraffin wax undergoes melting upon heating. The formation of a liquid surface layer is then followed by vaporization. Due to the low critical pressure of paraffin (6.5 bar [57]) it is possible to assume that the entrainment of liquid paraffin droplets into the main gas stream is part of the turbulent mixing process, and thus a dense fluid approach was used for the modeling of paraffin, using the properties provided in [58].

As described in [47], the fluid-surface interaction sub-model regarding pure paraffin is based on mass and energy balances, which reduce to

$$q_{w,\mathrm{conv}} + q_{w,\mathrm{rad}} = \dot{r} \cdot \rho_s \cdot \left[\Delta h_{\mathrm{melt}} + c_s \cdot (T_{\mathrm{melt}} - T_{s,\mathrm{in}})\right] \qquad (10)$$

where $q_{w,\mathrm{conv}}$ and $q_{w,\mathrm{rad}}$ are the convective and radiative wall heat fluxes, $\dot{r}$ the fuel regression rate, and the paraffin density, melting enthalpy, specific heat, melting temperature, and initial temperature are, respectively, $\rho_s = 929$ kg/m^3, $\Delta h_{\mathrm{melt}} = 169.83$ kJ/kg, $c_s = 1946.03$ J/(kg·K), $T_{\mathrm{melt}} = 343$ K and $T_{s,\mathrm{in}} = 298.15$ K.

The radiative heat flux is computed with an in-house code [47,59], which integrates the radiative heat transfer equations (RTE) for gray/diffuse boundaries and inhomogeneous gray/nonscattering media, using the DTM approach [60], in which a discretization of N_r rays is used to integrate the RTE with an integration step Δs. The evaluation of the radiative heat flux is carried out only at the boundaries and the sole emitting species considered are H_2O, CO_2 and CO. The wall emissivity is set to 0.91 and the refractive index to 1.43, according to the models proposed in [61,62].

Simulations taking into account the variation of fuel grain shape during the burning time have also been performed. This *shape change* approach simulates the entire firing test of the engine with a series of steady-state simulations in which the shape of the propellant grain is adjourned at each time step, taking into account the regression rate previously computed [63,50]. This approach is made possible by the characteristic times of grain regression being significantly larger than the ones of the gasdynamic and chemical phenomena inside the engine.

Table 2
Power law approximations (Eq. (3)) TOT and TR data. Thickness over time extends over the G_{ox} range 19 to 85 kg/(m^{2}s), while for TR, the investigated interval extends from 19 to 140 kg/(m^{2}s). Data are normalized with respect to those of pure paraffin obtained with DD reduction method, $a_{r,ref} = 0.126$ mm/(s·(kg/(m^2·s))$^{0.6}$).

Fuel Id.	Technique	No. of Tests	$a_r/a_{r,\mathrm{ref}}$	n_r	Data Fitting
F1	MB	8	1.413 ± 0.270	0.587 ± 0.049	0.941
	DD	8	1.000 ± 0.286	0.600 ± 0.071	0.921
	TR	8	1.127 ± 0.00(3)	0.567 ± 0.001	0.999
F2	DD	10	0.428 ± 0.048	0.648 ± 0.029	0.981
F5	DD	8	0.214 ± 0.024	0.729 ± 0.033	0.986
	TR	3	0.262 ± 0.00(1)	0.929 ± 0.001	0.988

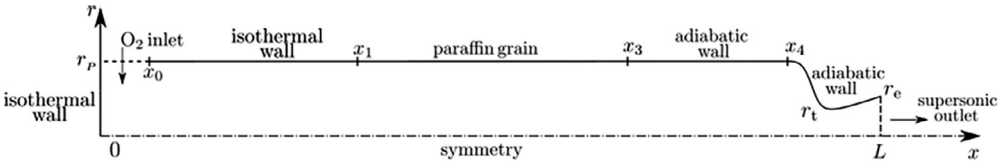

(a) Constant radius setup.

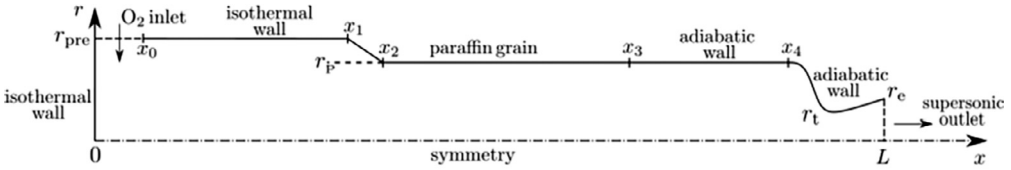

(b) Setup with prechamber cavity.

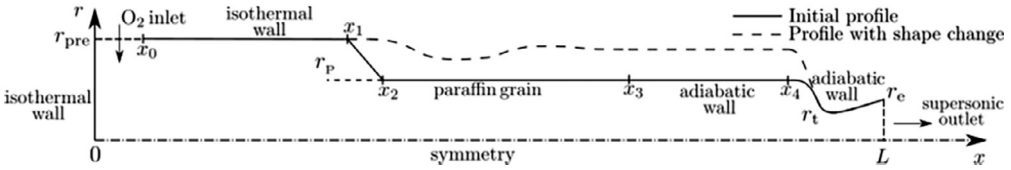

(c) Setup used for shape change simulations.

Fig. 3. Setups used for experimental rebuilding.

Table 3
Chemical reactions involved in the global reaction mechanism.

$C_{32}H_{66} \longrightarrow 16C_2H_4 + H_2$
$C_2H_4 + O_2 \longrightarrow 2CO + 2H_2$
$C_2H_4 + 2H_2O \longrightarrow 2CO + 4H_2$
$CO + H_2O \rightleftharpoons CO_2 + H_2$
$H_2 + \frac{1}{2}O_2 \rightleftharpoons H_2O$
$O_2 \rightleftharpoons 2O$
$H_2O \rightleftharpoons OH + H$

4. Computational setup

For the rebuilding of the experimental data different computational setups have been used, as shown in Fig. 3. All setups consist of a swirl injector ($0 < x < x_0$), a prechamber ($x_0 < x < x_1$), the paraffin grain ($x_1 < x < x_3$), a postchamber ($x_3 < x < x_4$), and a converging/diverging nozzle ($x_4 < x < L$). The latter is composed by conical sections connected by circular arcs with each other and with the cylindrical postchamber. In all setups the postchamber radius has been assumed equal to the port radius, since the postchamber affects mainly pressure and combustion efficiency, which are not the main focus of the present work.

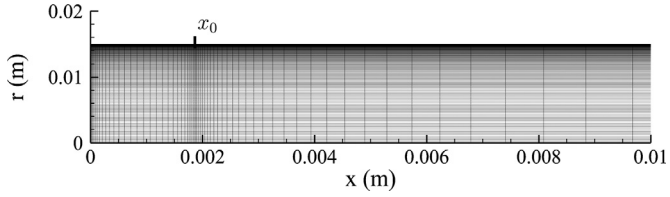

(a) Injection zone.

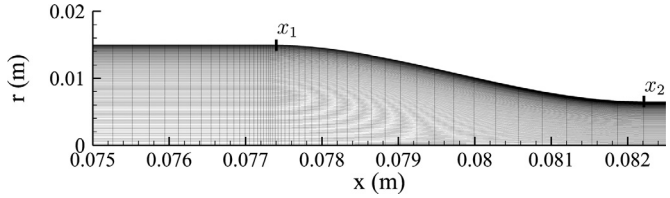

(b) Prechamber-grain transition.

Fig. 4. Details of the reference computational grid.

On the left-hand side an isothermal boundary condition is imposed, with temperature equal to the oxidizer injection temperature. The oxidizer injection is simulated with a subsonic inflow boundary condition, imposing mass flow rate and static temper-

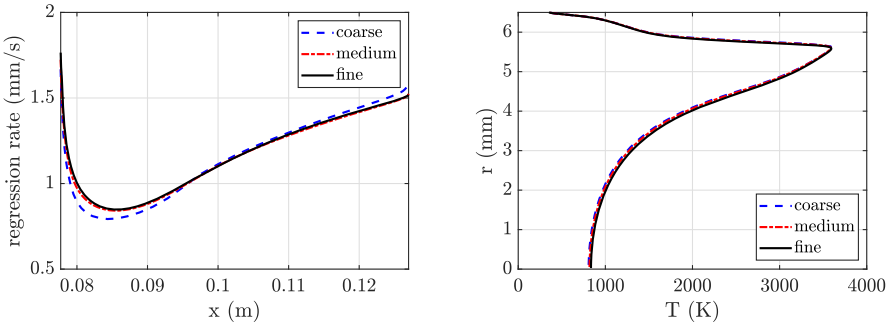

(a) Regression rate. (b) Temperature profile at middle grain.

Fig. 5. Results of the grid convergence analysis.

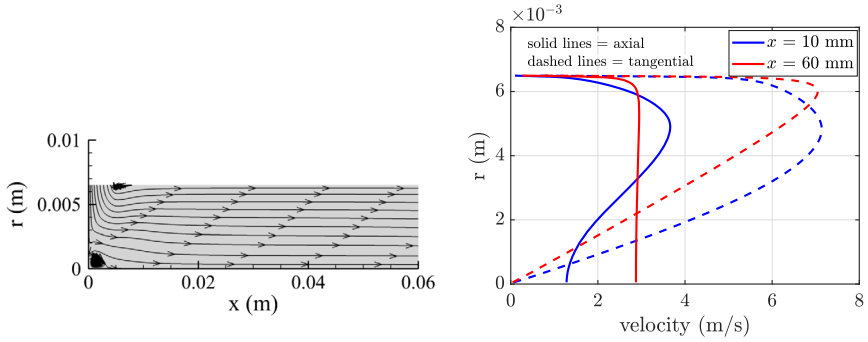

(a) Velocity streamlines. (b) Velocity profiles.

Fig. 6. Velocity streamlines and profiles in the prechamber for the $r_{pre} = r_p$ setup.

Table 4
Meshes considered for the grid refinement study.

	Coarse	Medium	Fine
Mesh	200 × 60	400 × 120	800 × 240
Number of control volumes	12000	48000	192000
Maximum cell height on grain (μm)	19.0	9.4	4.6
Maximum y^+ on grain	1.3	0.9	0.6

ature, with the discrete tangential injectors of the experimental setup substituted by an equivalent annular injector. In an axisymmetric approach it is not possible to inject the flow tangentially, thus either a radial or an axial injector has to be used. Given the geometry of the experimental setup it has been deemed more appropriate to inject the flow radially, but, being the prechamber long, it is expected that the effects of the injection arrangement on the fuel regression rate are small. The width of the injector has been chosen to match the experimental injection area and the flow injection angles are set to obtain a given geometric swirl number. The fuel grain boundary condition is based on the mass and energy balance equations, while the postchamber and nozzle walls are modeled with an adiabatic boundary condition. On the centerline a symmetry boundary condition is imposed and a supersonic outlet is assumed at nozzle exit. On the lateral faces a periodic boundary condition is set to model the axisymmetric swirling flow.

The first setup employed (Fig. 3(a)) assumes that the prechamber and the fuel grain have the same radius; the second, instead, takes into account the correct prechamber radius (Fig. 3(b)), modeling the prechamber-grain transition as an inclined line. When performing simulations accounting for the fuel grain shape change (Fig. 3(c)), the second setup has been employed, since it allows for a more precise comparison with the time-resolved experimental data. The prechamber-grain transition angle is set to 60°, as the

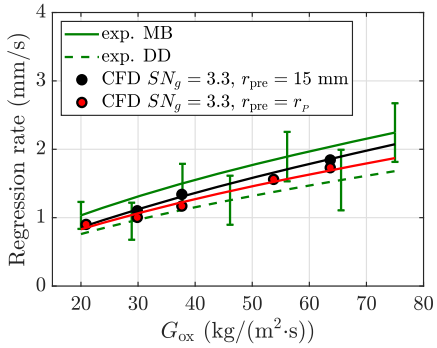

Fig. 7. Comparison between experimental and numerical data. Symbols represent the numerical average regression rates and lines their least square fit.

experimental results show that the inclination of the front-facing end of the grain varies between 90° and 45° during the burn.

Since the swirl intensity of the flow is directly proportional to the cross-sectional radius [28], a reduced swirl number SN_{inj} has to be imposed at the injector for the constant-radius setup. This allows approximating the swirl intensity reduction when the swirling flow moves from the prechamber to the fuel grain. Assuming that the flow is steady and inviscid the dependence of SN on the external radius is linear, resulting in

$$SN_{inj} = SN_g \cdot \frac{r_p}{r_{pre}} \tag{11}$$

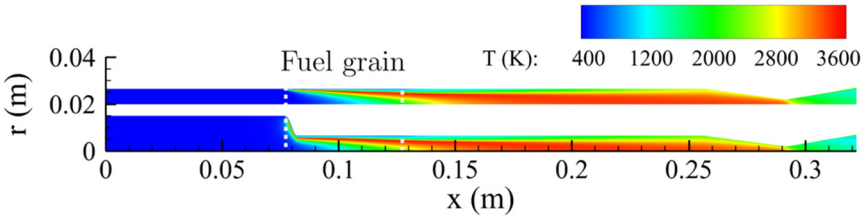

Fig. 8. Temperature flowfields for $r_p = 6.5$ mm, $SN_g = 3.3$. $r_{pre} = r_p$ (top), and $r_{pre} = 15$ mm (bottom).

Table 5
Comparison between fits of experimental and numerical data. The $a_r/a_{r,ref}$ coefficient is the same of Table 2. R^2 is the coefficient of determination.

Data	$a_r/a_{r,ref}$	n_r	R^2
Experimental MB	1.413	0.587	0.941
Experimental DD	1.000	0.600	0.921
Numerical $SN_g = 3.3$, $r_{pre} = 15$ mm	0.914	0.669	0.967
Numerical $SN_g = 3.3$, $r_{pre} = r_p$	1.042	0.615	0.972

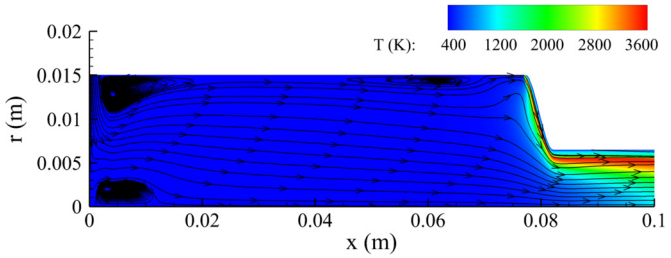

Fig. 9. Flowfield detail for $r_{pre} = 15$ mm, $r_p = 6.5$ mm, $SN_g = 3.3$.

5. Numerical results

In this section the numerical results are reported and compared with the experimental data. First, a convergence analysis of the computational grid and of the DTM discretization is reported (Sec. 5.1), then the numerical rebuilding of experimental data is performed (Sec. 5.2) using the three approaches previously explained. Finally, an analysis of the effect of swirl intensity on the fuel regression rate is performed in Sec. 5.3.

5.1. Grid convergence analysis

In this section the results of the grid convergence analysis are reported, considering the constant-radius setup. For the setup with prechamber cavity, a mesh with the same number of cells and similar topology has been employed, ensuring approximately the same wall resolution.

For all computations a structured grid made of 400×120 cells has been used, with clustering near the injector (Fig. 4a), at the grain leading edge (Fig. 4b), and at the nozzle throat. The convergence analysis has been performed using a coarse grid, made of 200 × 60 cells, and a fine grid of 800 × 240 cells.

The grid data are reported in Table 4, the local regression rate in Fig. 5(a) and the temperature profiles at middle grain in Fig. 5(b). On average, the average regression rate varies by 0.14% between the coarse and reference grid and only by 0.03% between the reference and fine grid, and the temperature profiles are almost superimposed. Therefore, the 400 × 120 grid is considered acceptable for all simulations.

A convergence analysis was performed also on the discretization used for the radiative heat flux evaluation, varying both the number or rays N_r and the integration step Δs. Considering $\Delta s = 1$ mm, the radiative heat flux on the grain varies on average by 0.3% increasing N_r from 144 to 256 and by 0.07% from 256 to 400. Fixing $N_r = 256$, the average variation of the radiative flux is 3.41% decreasing Δs from 5 mm to 1 mm and by 1.62% decreasing it from 1 mm to 0.5 mm. Based on these results, $N_r = 256$ and $\Delta s = 1$ mm were selected for all computations.

Fig. 6 shows the velocity streamlines in the prechamber, and the axial and tangential velocity profiles at two different sections for the $r_{pre} = r_p$ setup. The local flow field entailed by the specific injector arrangement is confined to the first part of the prechamber. Away from the injectors, the flow develops yielding a forced vortex (w proportional to r) with a decay of w close to the wall. This is consistent with three-dimensional numerical simulations and experimental data found in the literature [45,32]. For this reason, it is expected that the simplified injection approach employed in this work is able to correctly represent the internal ballistics entailed by the swirled flow.

5.2. Experimental rebuilding

In this section the rebuilding of the experimental data is performed. Simulations have been carried out for $SN_g = 3.3$ with r_p in the range $5 - 9.95$ mm, $\dot{m}_{ox}$ varying between 5 and 6.5 g/s, and employing both computational setups. The results are compared with the experimental data (Table 2) in Fig. 7 and Table 5.

Fig. 7 shows that the numerical results are generally inside the uncertainty bounds of the experimental data. The uncertainty on $\dot{r}$ is derived from the ones reported in Table 2 for a and n through error propagation analysis. The results obtained with the two setups are comparable, but the setup with the prechamber cavity yields higher regression rates, closer to the MB experimental values, since both the convective and radiative heat flux are influenced by the engine geometry, as will be discussed below. The simulations yield n values similar to the experimental ones, with the $r_{pre} = r_p$ law being very close to the experimental DD results. Indeed, simulations with $r_{pre} = r_p$ are expected to be more representative of the DD approach, as the contribution of the regression rate from the inclined surface at the grain's leading edge is not accounted for.

Fig. 8 compares the temperature fields obtained with the two setups. The flowfields are quite similar, but the higher regression rate for $r_{pre} = 15$ mm results in the formation of a wider cool gas layer near the wall, which reaches the nozzle throat. A detail of the prechamber is shown in Fig. 9. Near the injection two recirculation zones are created, one on the side of the injector and one on the axis, the former due to the radial injection of the oxidizer and the latter due to the centrifugal forces pushing the flow away from the centerline. The formation of a recirculation zone on the axis is expected at sufficiently high swirl intensities [28]. A third small vortex is formed just before the prechamber end near the wall. The flame is attached at the grain leading edge and quickly grows in thickness, reaching the engine axis just after the grain end ($x \approx 0.13$ m).

The local regression rates and the wall heat fluxes are compared in Fig. 10. For both simulations the regression rate closely follows the convective heat flux profile, although radiation accounts

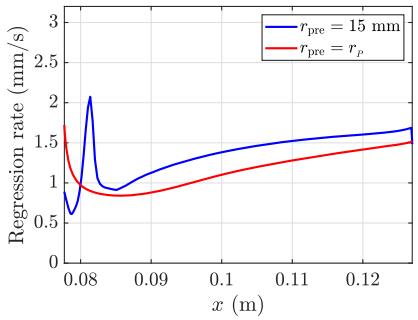

(a) Regression rate

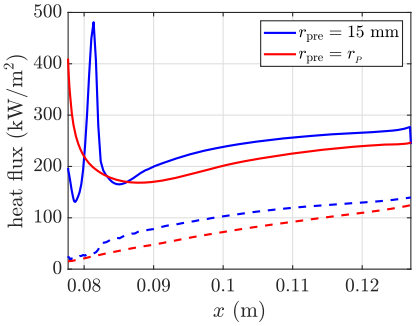

(b) Convective (solid lines) and radiative (dashed lines) heat flux over the fuel grain.

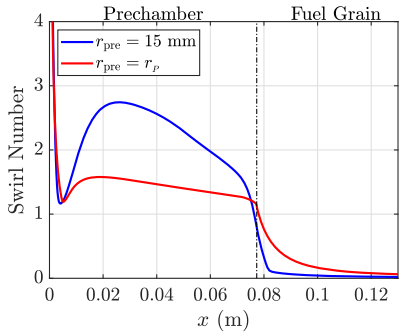

(c) Swirl Number.

Fig. 10. Effect of prechamber modeling on swirl number and wall heat flux.

for almost 35% of the total heat flux. In the constant-radius setup the convective heat flux first decreases and then increases, due to the combined effect of boundary layer growth and mass flux increase along the grain. In the setup with prechamber cavity an additional peak is present at $x \approx 0.081$ m, corresponding to the transition to the cylindrical section of the fuel grain. The radiative heat flux, instead, increases monotonically, as does the flame thickness (Fig. 8). The convective heat flux is higher when considering the prechamber cavity, because the burning surface is larger than in the constant-radius setup, which results in a higher mass flow rate and an increased convection. Additionally, the stronger blowing from the fuel surface results in a thicker flame, which explains the higher radiative heat flux.

It is interesting to compare also the swirl number variation along x between the two setups, as shown in Fig. 10(c). At $x = 0$, SN is almost infinite, since the oxidizer is injected radially and the denominator of Eq. (1) goes to zero if there is no mass flow rate. As the mass flow rate increases, the swirl number decreases and reaches a minimum, which is lower than the swirl number imposed at the injection, since the cross-section is reduced by the presence of the recirculation zones. After clearing the vortexes, the swirl intensity increases back to values close to the ones at the injection, and then decreases again, due to frictional decay. When the prechamber end is reached ($x = 77.3$ mm), the swirl intensity drops significantly, due to the effects of cross-section reduction, combustion and mass adduction, all of which increase the axial velocity u with respect to the tangential component w. The swirl intensity on the grain is lower for the setup with prechamber, since the larger fuel mass adduction results in a stronger swirl decay.

5.2.1. Shape change

To obtain a more precise rebuilding of the experimental data, one of the firing tests has been rebuilt also with the *shape change* approach. The test has an oxidizer mass flow rate of 6.5 g/s and an initial port diameter of 5 mm. Since the measures taken with the video equipment start at $r_p = 4$ mm, it has been chosen to start the simulations at this port radius, with a reduced burning time. The time intervals have been chosen according to the computed regression rate: the higher the regression the lower the time interval, for a total of 7 simulations, whose flowfields are shown in Fig. 11.

The computed grain profiles are reported in Fig. 12(a). The experimental and numerical axial consumption (computed at the grain leading edge) compare fairly well, with the predicted one lower by $\approx 15\%$. A slight error is, however, expected, since the mesh used is composed of a single computational block, instead of multiple blocks, which would be able to model a vertical wall.

In spite of the geometrical simplifications employed, there is a quite good agreement with the time-resolved data (Fig. 12(b) and 12(c)). The video camera allows to obtain the variation over time of the minimum grain diameter, from which also a regression rate trace can be derived. The regression rate computed at the minimum port radius compares fairly well with the TR data (Fig. 12(b)), being overestimated only at the first simulated burning time. Consequently, the minimum port radius is slightly overpredicted (Fig. 12(c)).

A final comparison has been made between the predicted and measured average pressure values. The experimental average value through the simulated time is 12.4 bar, while the time-average of the CFD simulations is 13.60 bar, with an error of $\approx 9.7\%$. The discrepancy between the two values can be explained by possible occlusions of the pressure sensor, and by the inability of the nu-

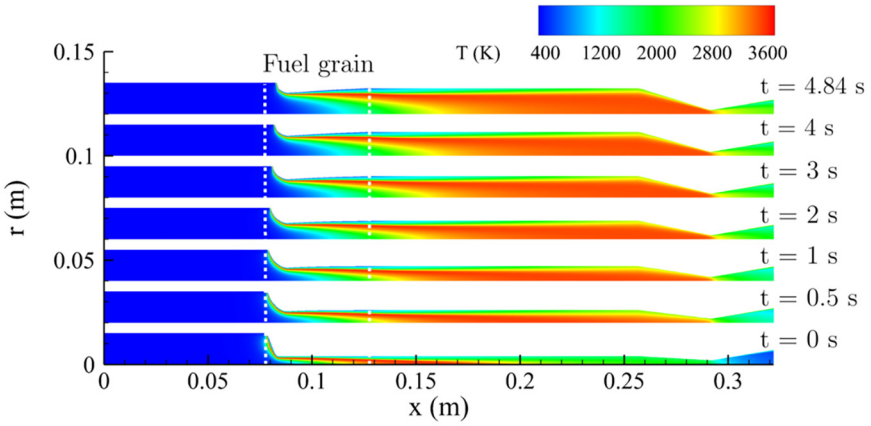

Fig. 11. Temperature flowfields for *shape change* simulations.

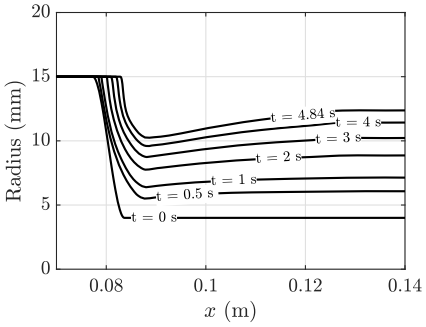

(a) Grain profile evolution.

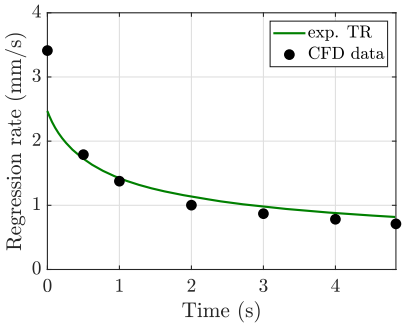

(b) Regression rate at point of minimum diameter.

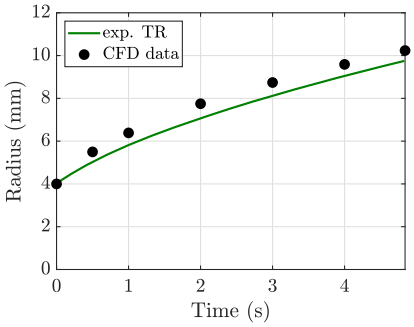

(c) Minimum grain diameter.

Fig. 12. Results of *shape-change* simulations.

merical approach to take into account the start-up transient of the engine, and the effect of the post-chamber cavity.

5.3. Effect of swirl on the regression rate

In this section an analysis of the effects of swirl on the fuel regression rate is performed. Twelve constant-radius simulations have been carried out at three port radii ($r_p = 5$, 6.5, 7.3 mm) and four swirl intensities ($SN_g = 0$, 1.1, 3.3, 9.9), employing the constant-radius setup of Fig. 3a. The oxidizer mass flow rate is $\dot{m}_{ox} = 5$ g/s.

The flowfields are shown in Fig. 13. As the swirl intensity increases, the main combustion zone shifts towards the grain leading edge, and the mean flow temperature in the postchamber decreases, since the increased regression rate results in fuel-rich mixture ratios. It can also be seen that a non-swirled flow results in a poor mixing and thin flame. By introducing swirl, instead, the improved mixing due to the lateral components of velocity yields a wider flame.

The regression rates are compared in Fig. 14(a) and the wall heat fluxes in Fig. 14(b). The convective and radiative heat flux show the same behavior of Fig. 10(b), and both increase with SN. Swirl intensity does not only raise the regression rate, but affects also its axial profile, moving its minimum towards the grain leading edge.

The average regression rates computed from the simulations have been fitted in a parametric law, in order to identify the dependencies of $\bar{\dot{r}}$ on SN. Assuming that the regression rate depends

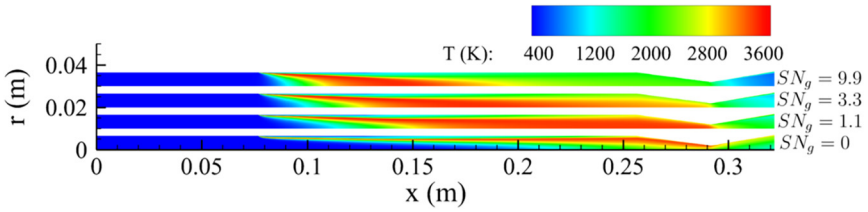

Fig. 13. Temperature flowfields with various swirl intensities and $r_p = 6.5$ mm.

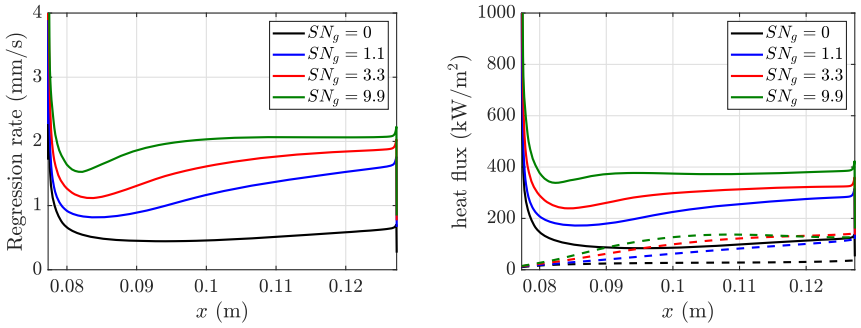

(a) Local regression rate for $r_P = 6.5$ mm. (b) Wall heat flux for $r_P = 6.5$ mm.

Fig. 14. Effect of swirl intensity on regression rate and wall heat flux.

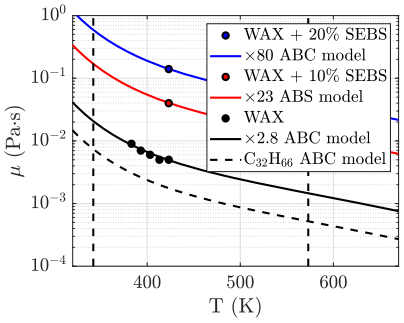

Fig. 15. Dynamic viscosity of F1, F2, and F5 fuel formulations from measurements (symbols) and model of [57] (dashed and solid lines). Vertical lines are the melting temperature (343 K) and the upper bound for the ABC model validity (573 K) [58].

only on the convective heat flux and that the Reynolds analogy holds for swirl flows, substituting the axial velocity with the total flow velocity [64], the selected law is $\bar{\dot{r}} = a_r \cdot \left(1 + SN_g^2\right)^{m_r} \cdot G_{ox}^{n_r}$. Moreover, it is assumed, as done in previous works [21,23], that the swirl number does not affect the value of n_r in the selected range of G_{ox}, hence $n_r = 0.615$ (from Table 5) is employed.

Fitting the data at all swirl intensities the correlation is

$$\bar{\dot{r}} = 0.0828 \left(1 + SN_g^2\right)^{0.2355} G_{ox}^{0.615} \text{ mm/s}, R^2 = 0.7760 \qquad (12)$$

Considering, instead, only the data at $SN_g = 1.1$, 3.3, 9.9 one gets

$$\bar{\dot{r}} = 0.1250 \left(1 + SN_g^2\right)^{0.1193} G_{ox}^{0.615} \text{ mm/s}, R^2 = 0.9498 \qquad (13)$$

The coefficient of determination R^2 is reported as a performance index of the laws. Eq. (13) fits the data much better than Eq. (12), suggesting how the selected correlation functional form might not able to model regression rates with axial and swirl injection at the same time.

6. SEBS-MA modeling

In this section an extension of the gas-surface interaction model (Sec. 3) to wax-SEBS fuel blends is derived, on the basis of a theoretical analysis and both numerical and experimental results.

The fuel regression rate computed through Eq. (10) depends on (i) the convective heat transfer; (ii) the radiative heat transfer; (iii) the fuel density ρ_s; (iv) the enthalpy of melting Δh_{melt}; (v) the conductive heat transfer $c_s(T_{melt} - T_{s,in})$. The convective heat transfer depends on the liquid isobaric specific heat, the dynamic viscosity, and the thermal conductivity (c_p, μ, k), while the radiative heat transfer depends on the grain radiation emissivity.

The effect of the addition of SEBS on the fuel density and the melting temperature has been observed to be negligible from experimental measurements (hence ρ_s, T_{melt}, $T_{s,in}$ are kept as the ones of F1 paraffin). Moreover, the radiation emissivity is not expected to influence significantly the regression rate [48].

The dynamic viscosities of the liquefied paraffin of the three formulations (F1, F2, F5) have been measured for different temperature ranges and are reported in Fig. 15. The asymptotic behavior correlation (ABC) values of [57] are multiplied by appropriate factors (2.8 for F1, 23 for F2, and 80 for F5) in order to reproduce the measured viscosities. Liquid specific heat and thermal conductivity were however not measured and are here assumed to be equal to the ones of the ABC model for all fuel formulations. The sensitivity of the regression rate to these two fuel properties has been assessed as negligible if they vary of 5-10%, which is expected given the dominance of paraffin in the fuel.

Properties of the solid fuel that strongly affect the regression rate in Eq. (10) are c_s and Δh_{melt}, which are however not known due to lack of experimental and literature data. The first one can be computed with a weighted average of wax and SEBS properties,

$$c_s = y_{SEBS} \cdot c_{s,SEBS} + (1 - y_{SEBS}) \cdot c_{s,wax} \qquad (14)$$

where $y_{SEBS} = 0$, 0.1, and 0.2 for F1, F2, and F5 formulations, respectively, and $c_{s,SEBS}$ is unknown.

Modeling of wax-SEBS blends should theoretically take into account the different nature of the two fuels (liquefying and pyrolyz-

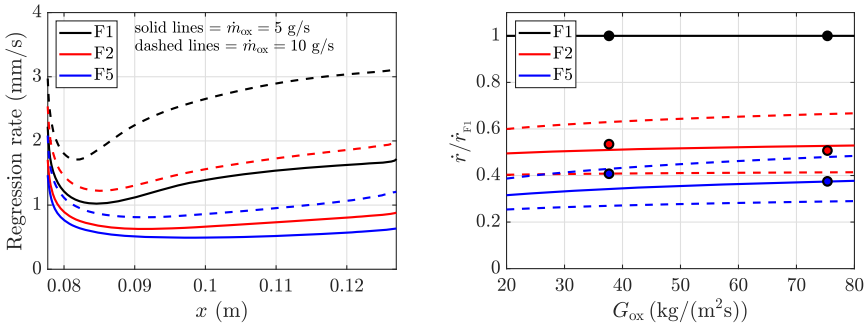

(a) Regression rate profiles over the fuel grain. (b) Regression rates normalized with the values obtained for the F1 formulation.

Fig. 16. Regression rates from simulations at $r_p = 6.5$ mm and $SN_g = 3.3$ for F1, F2, and F5 fuel formulations. In panel b) numerical results are shown with symbols, while lines indicate experimental nominal data (solid lines) with related uncertainty (dashed lines).

Table 6
Values of heat of pyrolysis Δh_p and specific heat c_s for different materials.

Material	Δh_p (MJ/kg)	c_s (J/(kg· K))	Reference
HTPB	1.1	1632.0	[65,66]
HDPE	2.72	1255.2	[67]
SEBS	4.624	2133.84	-

ing), which is outside the scope of this work. On the other hand, in order to compute Δh_{melt}, it is here assumed that the pyrolysis of SEBS takes place simultaneously to the melting of the paraffin grain. In this way, Δh_{melt} is obtained as a weighted average of the heat of melting of paraffin and the heat of pyrolysis of SEBS,

$$\Delta h_{melt} = y_{SEBS} \cdot \Delta h_p + (1 - y_{SEBS}) \cdot \Delta h_{melt,wax} \tag{15}$$

where Δh_p is unknown.

Due to lack of experimental and literature data, SEBS values of c_s and Δh_p are inferred from comparison between CFD results and experimental data. The main tuning parameter is the term on the right hand side of Eq. (10), which reads

$$\Delta H = \Delta h_{melt} + c_s \cdot (T_{melt} - T_{s,in}) \tag{16}$$

Four different simulations at port radius 6.5 mm and $SN_g = 3.3$ were performed, resulting in the regression rates shown in Fig. 16a. By normalizing the regression rates with the ones obtained with the F1 formulation, it was possible, by adopting $\Delta H_{SEBS} = 1.7 \Delta H_{HDPE}$, to fit the data through the experimental trends with good accuracy (Fig. 16b). It is remarkable that, despite of the modeling assumptions, a single tuning of ΔH yields an acceptable representation of the regression rate for two different fuel formulations and oxidizer mass flow rates. The individual values of Δh_p and c_s are such that $\Delta H_{SEBS} = 1.7 \Delta H_{HDPE}$ and are reported in Table 6, where they can be compared with properties of HTPB and HDPE.

A final consideration is to be given to the chemical composition of the liquefied fuel. To model exactly the behavior of wax-SEBS fuels one should consider not only paraffin, but also styrene (C_8H_8), ethylene (C_2H_4), and butylene (C_4H_8). However, considering the relatively low mass fraction of styrene present in SEBS-MA [68], the overall ratio between carbon and hydrogen atoms is not significantly modified with respect to pure paraffin. Therefore, it is assumed that the only species released from the fuel to the flowfield is $C_{32}H_{66}$. A simulation considering the injection of 10% ethylene with 90% $C_{32}H_{66}$ provided no appreciable change in regression rate with respect to a simulation considering 100% $C_{32}H_{66}$ injection.

Combining the results of this analysis with the experimental data of Sec. 2, the parametric law of Sec. 5.3 can be extended to wax-SEBS fuel blends. Assuming that the fuel composition affects only the a coefficient, a correction factor can be introduced to account for the regression rate decrease from pure wax to the F2 and F5 fuel formulations. From the data reported in Fig. 16b, considering the two simulated oxidizer mass fluxes, the average values of such coefficient are 0.52 and 0.39 for the F2 and F5 fuel formulations, respectively.

7. Conclusions

In this work an experimental and numerical analysis of a lab-scale hybrid rocket engine burning paraffin-wax and gaseous oxygen has been performed in order to assess the effect of swirl injection on the regression rate.

Tested specimens featured grain lengths of 50 mm, with external diameter of 30 mm and initial port diameter in the range 5 to 20 mm. Firing tests were conducted varying oxygen mass flow rate from 5 to 10 g/s, obtaining average oxidizer mass fluxes in the range 20-60 kg/(m^2·s) and regression rates in the range 0.5 to 2.5 mm/s. Regression rates obtained by classical thickness-over-time (TOT) averaging procedure were compared to fuel time-resolved ballistics. Time-resolved data were obtained by an optical method enabling port diameter tracking.

A numerical axisymmetric RANS approach has been employed for the rebuilding of experimental data at different oxidizer mass fluxes and mass flow rates, yielding satisfactory results. The predictive capabilities of the model have been improved through simulations taking into account the variation of the fuel grain shape during the burn. Moreover, a simplified approach has been employed for the modeling of paraffin fuels with SEBS additives.

A parametric analysis, performed varying both the port radius and the swirl intensity, has allowed to assess the effect of swirl intensity on both the average and the local regression rate. A parametric law linking the average regression rate to the oxidizer mass flux and the swirl number has also been found.

Declaration of competing interest

The authors declare that they have no known competing financial interests or personal relationships that could have appeared to influence the work reported in this paper.

Data availability

Data will be made available on request.

Acknowledgements

This work is part of a wider research framework on hybrid rocket propulsion funded by the Italian Space Agency under contract ASI N. 2019-5-I.0, CUP F84E16002240003.

References

[1] G.P. Sutton, O. Biblarz, Rocket Propulsion Elements, John Wiley and Sons, Inc., 2017.
[2] M.J. Chiaverini, K.K. Kuo (Eds.), Fundamentals of Hybrid Rocket Combustion and Propulsion, AIAA, 2007.
[3] D. Pastrone, Approaches to low fuel regression rate in hybrid rocket engines, Int. J. Aerosp. Eng. (2012) 2012, https://doi.org/10.1155/2012/649753.
[4] B. Cantwell, A. Karabeyoglu, D. Altman, Recent advances in hybrid propulsion, Int. J. Energ. Mater. Chem. Propuls. 9 (2010) 305–326, https://doi.org/10.1615/IntJEnergeticMaterialsChemProp.v9.i4.20.
[5] C. Schmierer, M. Kobald, U. Fischer, K. Tomilin, A. Petrarolo, F. Hertel, Advancing Europe's hybrid rocket engine technology with paraffin and LOX, in: 8th European Conference for Aeronautics and Space Sciences (EUCASS), 2019.
[6] Project: HYPROGEO, EC H2020 Project Number 634534, Hybrid Propulsion Module for Transfer to GEO Orbit, 2015 – 2018.
[7] J.Y. Lestrade, J. Anthoine, A. Musker, A. Lecossais, Experimental demonstration of an end-burning swirling flow hybrid rocket engine, Aerosp. Sci. Technol. 92 (2019) 1–8, https://doi.org/10.1016/j.ast.2019.05.057.
[8] M. Faenza, A. Boiron, B. Haemmerli, S. Lennart, T. Vesteras, O. Verberne, Getting ready for space: Nammo's development of a 30 kN hybrid rocket based technology demonstrator, in: 7th European Conference for Aeronautics and Space Sciences (EUCASS), 2017.
[9] M.A. Karabeyoglu, D. Altman, B.J. Cantwell, Combustion of liquefying hybrid propellants: part 1, general theory, J. Propuls. Power 18 (3) (2002) 610–620, https://doi.org/10.2514/2.5975.
[10] M.A. Karabeyoglu, B. Cantwell, D. Altman, Development and testing of paraffin-based hybrid rocket fuels, in: 37th Joint Propulsion Conference and Exhibit, 2001.
[11] M. Kobald, C. Schmierer, H.K. Ciezki, S. Schlechtriem, E. Toson, L.T. De Luca, Viscosity and regression rate of liquefying hybrid rocket fuels, J. Propuls. Power 33 (5) (2017) 1245–1251, https://doi.org/10.2514/1.B36207.
[12] C. Paravan, L. Galfetti, F. Maggi, A critical analysis of paraffin-based fuel formulations for hybrid rocket propulsion, in: 53rd AIAA/SAE/ASEE Joint Propulsion Conference 2017, AIAA Paper 2017-4830 https://doi.org/10.2514/6.2017-4830.
[13] Y. Wu, X. Yu, X. Lin, S. Li, X. Wei, C. Zhu, et al., Experimental investigation of fuel composition and mix-enhancer effects on the performance of paraffin-based hybrid rocket motors, Aerosp. Sci. Technol. 82 (83) (2018) 620–627, https://doi.org/10.1016/j.ast.2018.09.026.
[14] Y. Tang, S. Cheng, W. Zhang, R. Shen, L. DeLuca, Y. Ye, Mechanical modifications of paraffin-based fuels and the effects on combustion performance, Propellants Explos. Pyrotech. 42 (11) (2017) 1268–1277, https://doi.org/10.1002/prep.201700136.
[15] J. Thomas, C. Paravan, J. Stahl, A. Tykol, F. Rodriguez, L. Galfetti, et al., Experimental evaluation of HTPB/paraffin fuel blends for hybrid rocket applications, Combust. Flame 229 (2021) 111386, https://doi.org/10.1016/j.combustflame.2021.02.032.
[16] S. Yuasa, O. Shimada, T. Imamura, T. Tamura, K. Yamoto, A technique for improving the performance of hybrid rocket engines, in: 35th Joint Propulsion Conference and Exhibit, 1999.
[17] C. Lee, Y. Na, J.W. Lee, Y.H. Byun, Effect of induced swirl flow on regression rate of hybrid rocket fuel by helical grain configuration, Aerosp. Sci. Technol. 11 (1) (2007) 68–76, https://doi.org/10.1016/j.ast.2006.07.006.
[18] C. Palani Kumar, A. Kumar, Effect of swirl on the regression rate in hybrid rocket motors, Aerosp. Sci. Technol. (2013) 29, https://doi.org/10.1016/j.ast.2013.01.011.
[19] T. Sakurai, S. Yuasa, H. Ando, K. Kitagawa, T. Shimada, Performance and regression rate characteristics of 5-kN swirling-oxidizer-flow-type hybrid rocket engine, J. Propuls. Power 33 (4) (2017) 891–901, https://doi.org/10.2514/1.B36239.
[20] M. Bouziane, A. Bertoldi, P. Milova, P. Hendrick, M. Lefebvre, Performance comparison of oxidizer injectors in a 1-kN paraffin-fueled hybrid rocket motor, Aerosp. Sci. Technol. 89 (2019) 392–406, https://doi.org/10.1016/j.ast.2019.04.009.
[21] F.D.A. Quadros, P.T. Lacava, Swirl injection of gaseous oxygen in a lab-scale paraffin hybrid rocket motor, J. Propuls. Power 35 (5) (2019) 896–905, https://doi.org/10.2514/1.B37283.
[22] L.l. Liu, X. He, Y. Wang, Z.b. Chen, Q. Guo, Regression rate of paraffin-based fuels in hybrid rocket motor, Aerosp. Sci. Technol. 107 (2020) 106269, https://doi.org/10.1016/j.ast.2020.106269.
[23] M. Franco, F. Barato, E. Paccagnella, M. Santi, A. Battiston, A. Comazzetto, et al., Regression rate design tailoring through vortex injection in hybrid rocket motors, J. Spacecr. Rockets 57 (2) (2020) 278–290, https://doi.org/10.2514/1.A34539.
[24] W. Li, X. Chen, D. Zhao, B. Wang, K. Ma, T. Cai, Swirling effect on thermodynamic performance in a solid fueled ramjet with paraffin-polyethylene, Aerosp. Sci. Technol. 107 (2020) 106341, https://doi.org/10.1016/j.ast.2020.106341.
[25] G. Cai, Z. Zhao, B. Zhao, Y. Liu, N. Yu, Regression rate and combustion performance investigation on hybrid rocket motor with head-end swirl injection under high geometric swirl number, Aerosp. Sci. Technol. 103 (2020) 105922, https://doi.org/10.1016/j.ast.2020.105922.
[26] Z. Zhang, X. Lin, Z. Wang, K. Wu, J. Luo, S. Fang, et al., Effects of swirl injection on the combustion of a novel composite hybrid rocket fuel grain, Acta Astronaut. 199 (2022) 174–182, https://doi.org/10.1016/j.actaastro.2022.07.027.
[27] F. Chang, V. Dhir, Mechanisms of heat transfer enhancement and slow decay of swirl in tubes using tangential injection, Int. J. Heat Fluid Flow 16 (2) (1995), https://doi.org/10.1016/0142-727X(94)00016-6.
[28] A.K. Gupta, D.G. Lilley, N. Syred, Swirl Flows, Abacus Press, 1984.
[29] G.P. Sutton, History of Liquid Propellant Rocket Engines, AIAA, 2006.
[30] N. Syred, J. Beér, Combustion in swirling flows: a review, Combust. Flame 23 (2) (1974), https://doi.org/10.1016/0010-2180(74)90057-1.
[31] T. Claypole, N. Syred, The effect of swirl burner aerodynamics on NOx formation, in: 18th Symposium (International) on Combustion, 1981.
[32] F. Chang, V. Dhir, Turbulent flow field in tangentially injected swirl flows in tubes, Int. J. Heat Fluid Flow 15 (5) (1994), https://doi.org/10.1016/0142-727X(94)90048-5.
[33] K. Ozawa, T. Shimada, Linear combustion stability analysis of uni-directional vortex injection hybrid rocket engines, in: 50th AIAA/ASME/SAE/ASEE Joint Propulsion Conference, 2014.
[34] D.R. Greatrix, Geometric swirl number and hybrid rocket engine performance, in: 2018 Joint Propulsion Conference, 2018.
[35] S. Yuasa, N. Shiraishi, K. Hirata, Controlling parameters for fuel regression rate of swirling-oxidizer-flow-type hybrid rocket engine, in: 48th AIAA/ASME/SAE/ASEE Joint Propulsion Conference, 2012.
[36] B. Vignesh, R. Kumar, Effect of multi-location swirl injection on the performance of hybrid rocket motor, Acta Astronaut. 176 (2020) 111–123, https://doi.org/10.1016/j.actaastro.2020.06.029.
[37] A. Reina, M. Frezzotti, G. Mangioni, A. Cretella, F. Battista, L. Galfetti, et al., Hybrid propulsion system for future rocket applications, in: 2022 Space Propulsion Conference, 2022.
[38] C. Paravan, L. Galfetti, R. Bisin, F. Piscaglia, Combustion processes in hybrid rockets, Int. J. Energ. Mater. Chem. Propuls. 18 (3) (2019) 255–286, https://doi.org/10.1615/intjenergeticmaterialschemprop.2019027834.
[39] C. Paravan, Nano-sized and mechanically activated composites: perspectives for enhanced mass burning rate in aluminized solid fuels for hybrid rocket propulsion, Aerospace 12 (6) (2019) 1–31, https://doi.org/10.3390/aerospace6120127.
[40] R. Bisin, C. Paravan, A new strategy for the reinforcement of paraffin-based fuels based on cellular structures: the armored grain — ballistic characterization, Acta Astronaut. 206 (2023) 284–298, https://doi.org/10.1016/j.actaastro.2023.02.027.
[41] C. Paravan, M. Manzoni, G. Rambaldi, L.T. DeLuca, Analysis of quasi-steady and transient burning of hybrid fuels in a lab-scale burner by an optical technique, Int. J. Energ. Mater. Chem. Propuls. 13 (5) (2013) 385–410.
[42] R. Bisin, C. Paravan, S. Alberti, L. Galfetti, A new strategy for the reinforcement of paraffin-based fuels based on cellular structures: the armored grain — mechanical characterization, Acta Astronaut. 176 (2020) 494–509, https://doi.org/10.1016/j.actaastro.2020.07.003.
[43] J.D. Anderson, Hypersonic and High-Temperature Gas Dynamics, AIAA Education Series, 2006.
[44] N. Bellomo, F. Barato, M. Faenza, M. Lazzarin, A. Bettella, D. Pavarin, Numerical and experimental investigation of unidirectional vortex injection in hybrid rocket engines, J. Propuls. Power 29 (5) (2013) 1097–1113, https://doi.org/10.2514/1.B34506.
[45] E. Paccagnella, F. Barato, D. Pavarin, A. Karabeyoğlu, Scaling parameters of swirling oxidizer injection in hybrid rocket motors, J. Propuls. Power 33 (6) (2017) 1378–1394, https://doi.org/10.2514/1.B36241.
[46] M. Motoe, T. Shimada, Numerical simulations of combustive flows in a swirling-oxidizer-flow-type hybrid rocket, in: 52nd Aerospace Sciences Meeting, 2014.
[47] M.T. Migliorino, D. Bianchi, F. Nasuti, Numerical analysis of paraffin-wax/oxygen hybrid rocket engines, J. Propuls. Power 36 (6) (2020) 806–819, https://doi.org/10.2514/1.B37914.
[48] M.T. Migliorino, D. Bianchi, F. Nasuti, Numerical simulations of the internal ballistics of paraffin–oxygen hybrid rockets at different scales, Aerospace 8 (8) (2021), https://doi.org/10.3390/aerospace8080213.
[49] D. Bianchi, B. Betti, F. Nasuti, C. Carmicino, Simulation of gaseous oxygen/hydroxyl-terminated polybutadiene hybrid rocket flowfields and comparison with experiments, J. Propuls. Power 31 (3) (2015) 919–929, https://doi.org/10.2514/1.B35587.
[50] M.T. Migliorino, G. Gubernari, D. Bianchi, F. Nasuti, D. Cardillo, F. Battista, Numerical simulations of fuel shape change in paraffin–oxygen hybrid rocket engines, J. Propuls. Power (2023) 1–15, https://doi.org/10.2514/1.B39086, published online (article in advance).

[51] P. Roe, Approximate Riemann solvers, parameter vectors, and difference schemes, J. Comput. Phys. 43 (2) (1981) 357–372, https://doi.org/10.1016/0021-9991(81)90128-5.
[52] G. Strang, On the construction and comparison of difference schemes, SIAM J. Numer. Anal. 5 (3) (1968) 506–517, https://doi.org/10.1137/0705041.
[53] B.J. McBride, M.J. Zehe, Gordon S. NASA Glenn coefficients for calculating thermodynamic properties of individual species, NASA TP-2002-211556, 2002.
[54] P. Spalart, S. Allmaras, A One-Equation Turbulence Model for Aerodynamic Flows, AIAA, 1992, p. 439.
[55] B.M. Fabuss, J.O. Smith, R.I. Lait, A.S. Borsanyi, C.N. Satterfield, Rapid thermal cracking of n-hexadecane at elevated pressures, Ind. Eng. Chem. Process Des. Dev. 1 (4) (1962) 293–299, https://doi.org/10.1021/i260004a011.
[56] B. Blouri, F. Hamdan, D. Herault, Mild cracking of high-molecular-weight hydrocarbons, Ind. Eng. Chem. Process Des. Dev. 24 (1) (1985) 30–37, https://doi.org/10.1021/i200028a005.
[57] J.J. Marano, G.D. Holder, General equation for correlating the thermophysical properties of n-paraffins, n-olefins, and other homologous series. 2. Asymptotic behavior correlations for pvt properties, Ind. Eng. Chem. Res. 36 (5) (1997) 1895–1907, https://doi.org/10.1021/ie960512f.
[58] J.J. Marano, G.D. Holder, A general equation for correlating the thermophysical properties of n-paraffins, n-olefins, and other homologous series. 3. Asymptotic behavior correlations for thermal and transport properties, Ind Eng Chem Res 36 (6) (1997) 2399–2408, https://doi.org/10.1021/ie9605138.
[59] G. Leccese, D. Bianchi, B. Betti, D. Lentini, F. Nasuti, Convective and radiative wall heat transfer in liquid rocket thrust chambers, J. Propuls. Power 34 (2) (2018) 318–326, https://doi.org/10.2514/1.B36589.
[60] H. Versteeg, W. Malalasekera, An Introduction to Computational Fluid Dynamics, Pearson Education, 2007.
[61] G.M. Carlomagno, T. Astarita, Infrared Thermography for Thermo-Fluid-Dynamics, Springer, ISBN 978-3-642-29507-2, 2013.
[62] F. Mark, J.I. Kroschwitz, Encyclopedia of Polymer Science and Engineering, vol. 17, John Wiley & Sons, 1989.
[63] M.T. Migliorino, G. Gubernari, D. Bianchi, F. Nasuti, D. Cardillo, F. Battista, Numerical simulations of fuel shape change in paraffin-oxygen hybrid rocket engines, in: AIAA Aviation Forum, 2022.
[64] R.F. Lopina, A.E. Bergles, Heat transfer and pressure drop in tape-generated swirl flow of single-phase water, J. Heat Transf. 91 (3) (1969) 434–441, https://doi.org/10.1115/1.3580212.
[65] K. Ramohalli, J. Yi, Hybrids revisited, in: 26th Joint Propulsion Conference and Exhibit, 1990.
[66] E. Farbar, J. Louwers, T. Kaya, Investigation of metallized and nonmetallized hydroxyl terminated polybutadiene/hydrogen peroxide hybrid rockets, J. Propuls. Power 23 (2) (2007) 476–486, https://doi.org/10.2514/1.22091.
[67] G. Lengelle, B. Fourest, J. Godon, C. Guin, Condensed-phase behavior and ablation rate of fuels for hybrid propulsion, in: 29th Joint Propulsion Conference and Exhibit, 1993.
[68] Z.M. Kusmono, W. Chow, T. Takeichi, Rochmadi, Compatibilizing effect of SEBS-g-MA on the mechanical properties of different types of OMMT filled polyamide 6/polypropylene nanocomposites, Composites, Part A, Appl. Sci. Manuf. 39 (12) (2008) 1802–1814, https://doi.org/10.1016/j.compositesa.2008.08.009.